On the turbulent flow models in modelling of omni-flow wind turbine

YK Chen[*], P Ying, Y Xu and Y Tian

University of Hertfordshire, School of Engineering and Technology, Hatfield, Herts. AL10 9AB, UK, y.k.chen@herts.ac.uk

Abstract - The computational fluid dynamics (CFD) has a wide application in the wind energy industry. In CFD simulations, a turbulence model plays a significantly important role in accuracy and resource cost. In this paper, a novel wind turbine, omni-flow wind turbine, was investigated with different turbulence models. Four turbulence models, standard k-ε, realizable k-ε, standard k-ω and SST k-ω models, were employed for this wind turbine in order to assess the best numerical configuration. The performance of these four turbulence models was validated with wind tunnel tests. It is evident that the realizable k-ε turbulence model is most suitable to simulate this novel wind turbine.

Keywords: CFD, Omni-flow wind turbine, Turbulence model

1. Introduction

Worldwide interest in renewable energy options has given rise to emergence of new wind turbine designs. Wind energy can be converted to a maximum of fifty nine per cent of useful wind energy according to the Betz limit [1]. Wind turbines can be categorized into large and small according to size. Generally, large wind turbines are constructed in wide space for many users. High rise towers, long blades, heavy weight and big power are the major features. These wind turbines have high space requirements and wind energy source. For small wind turbines Clausen & Wood [2-5] divided them into three categories: micro, mid-range, and mini wind turbines. The radius of a micro wind turbine is less than 1.5 meter and the power is less than 1 kW. It is suitable to construct on the tops of buildings. In an urban area, the wind velocity on the top is higher than that on ground. Rich wind energy can compensate electricity consumption of high buildings by wind turbines for economical and environmental protection purposes. It is valuable to develop an efficient small wind turbine for urban areas.

There are different types of wind turbines and two main categories of them are vertical and horizontal axis wind turbines. The axis is also stating the direction that the turbine is encountering the wind. Vertical axis wind turbines were initially started as drag devices (Savonious) and only recently researchers have given emphasis into the lift driven vertical axis wind turbines. The lift driven wind turbines were proposed by a French engineer, Darrieus, in 1925 [6]. Vertical axis wind turbines are described in three fundamental types: i) Savonious wind turbines; ii) Darrieus wind turbines, iii) Giromill or H-Rotor wind turbines. The common feature of all types of vertical axis wind turbines is that the main rotor shaft is arranged vertically. It can take advantage of any wind direction and it is vital where wind shifts direction or where turbulence flow exists. Vertical rotors do not require a yawing mechanism for accepting the wind from any direction with less moving parts and in addition it can provide direct rotary drive to a fixed load [7]. All the components (including mechanical and electrical components) that require maintenance are located at the ground level providing easier and faster access compromising reduced costs for maintenance [6].

The main drawback for the vertical axis wind turbines is the non-self-starting capability. Many researches though-out the years have been conducted for an elucidation of the problem, with a more resent research, the use of cambered airfoils on a straight bladed Darrieus type vertical axis wind turbine [4]. In addition the low tip speed ratios are considered to be a drawback and not being able to control the power output by pitching the rotor blades.
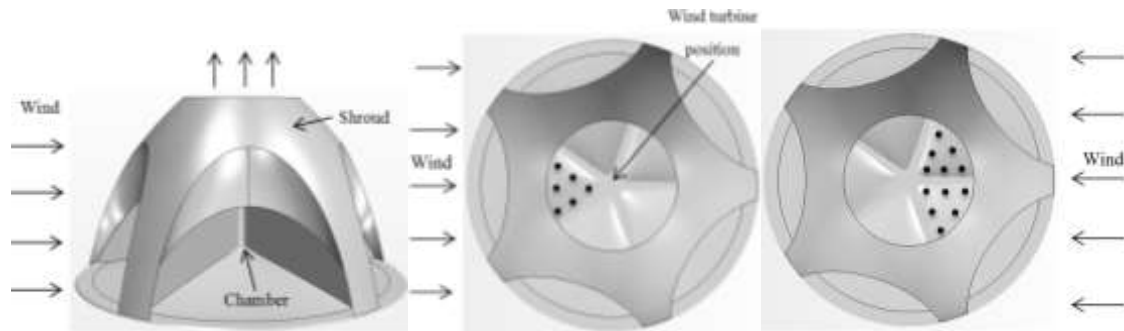

Figure 1: A typical shroud of the omni-flow wind energy system: (a) schematic; (b) under different entrance flow of wind [3]

A novel omni-flow wind energy system was proposed for urban areas [8]. The aerodynamic characteristics of such a wind energy system were studied by Zhang [3] who performed computational fluid dynamics (CFD) analyses and experiments. Fig. 1 shows a typical 3-D model of this system. The system consists of five chambers, which are located along the circumference of the shroud and form a vertical passage for entrainment of flow of the incoming wind. The omni-flow wind energy system was designed to better receive approaching wind from all directions, and to effectively transmit the wind to the air turbine located downstream. With this feature, the omni-flow wind energy system can cater for a wide variety of varying wind conditions. The velocities of the approaching wind can also be significantly accelerated due to the contraction of the nozzle structure. However, since the air flow only passes through one or two of the five chambers at any given time, as shown in Fig.1(b), the flow velocity distribution in front of the turbine is not uniform. Hence, the blades are under different flow velocities and as a consequence, undergo different aerodynamic loads during one operation cycle. Therefore it is difficult for a wind turbine with conventional thin blades to accommodate the flow conditions in the omni-flow wind energy system.

A new type of wind turbine blade for omniflow wind turbine has been designed based upon the impulse turbine principles. However, there is little information on whether impulse turbine principles could be applied to a wind turbine. It is essential to numerically investigate the aerodynamic features of a wind turbine based on impulse turbine principles.

The aim of this paper is to numerically investigate the aerodynamic features of a wind turbine based on impulse turbine principles. Four turbulence models, standard k-ε, realizable k-ε standard k-ω and SST k-ω models, were employed for this wind turbine in order to assess the best numerical configuration. The performance of these four turbulence models was validated with the results from wind tunnel tests.

2. The Wind Turbine Model

As shown in Fig. 2, the wind turbine consists of two components: a stator with guide vanes and a rotor with blades. Wind flow approaches the stator first and then leads to the rotor with the guide vanes. The omni-flow wind turbine is designed to work at the exit chamber of the shroud. Guide vanes are fixed to the surrounding wall of the exit chamber. As shown in Fig. 2(b), the guide vanes have thin plate geometry. The front part of a guide vane takes the shape of an arc and the rear part is straight. The straight part has a setting angle of 20o. Due to the geometric feature of the guide vanes, the flow velocity of the approaching wind will be accelerated. Meanwhile, the flow direction is also changed as a function of the setting angle of the rear part of the vane.
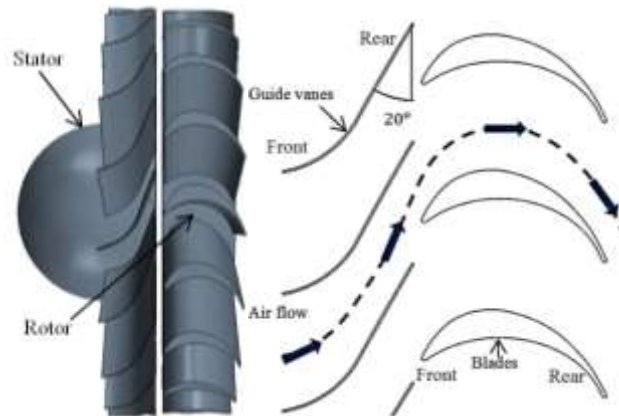

Figure 2: A Schematic view of the wind turbine: (a) 3D view of the turbine model; (b) schematic view of guide vanes and blades [4].

The blades on the rotor used an aerofoil of the type found in a unidirectional impulse turbine. The rationale for using this type of blade aerofoil, was that it has the best power performance compared with other blade aerofoils in wave energy [10]. Based upon the sketch from Maeda et al [11], a further change of the blade aerofoil has been incorporated. Compared with conventional HAWTs, the omni-flow wind turbine employs a larger hub-to-tip ratio, which is defined as the hub diameter over blade diameter. The amount of the maximum aerofoil camber takes a 36% of the chord which is also larger than 0-6% of commonly used NACA aerofoils [12].

3. Aerodynamic Analysis of the Wind Turbine

The omni-flow wind turbine was analysed by the blade element method, which is commonly used for the calculation of aerodynamic loads on blades and the power output of a wind turbine [13-14]. This method refers to an analysis of forces at a section of the blade. For this wind turbine, the wind velocity diagram is shown in Fig. 3(a). U is the free-stream wind velocity, U_1 is the velocity of the flow after passing guide vanes, V_r represents the tangential velocity of a blade at the radius r of an element and W is the relative wind velocity. The relationship between these velocities is shown below:

$$\vec{W} = \vec{U_1} + \vec{V_r} \tag{1}$$

The relative wind velocity is lower than the velocity of the flow after passing guide vanes. A force diagram of the blade aerofoil is shown in Fig. 3(b).

The tangential force F_T on the blade element can be expressed as

$$dF_T = dF_L \cos\phi + dF_D \sin\phi \tag{2}$$

and the axial force, F_N can be given by,

$$dF_N = -dF_L \sin\phi + dF_D \cos\phi \tag{3}$$

where F_L and F_D represent lift and drag respectively, and ϕ is the angle between the relative velocity and the rotating axis. It should be noted that both lift and drag forces contribute to the tangential force in this case as such wind turbine is driven by dual forces: lift and drag.

The torque T on an element can be calculated as follows:

$$dT = Nr\,(dF_L \cos\phi + dF_D \sin\phi) \tag{4}$$

where N denotes the total number of blades.

The power output P on an element can then be expressed as

$$dP = \omega dT \tag{5}$$

where is the angular speed of the rotor.

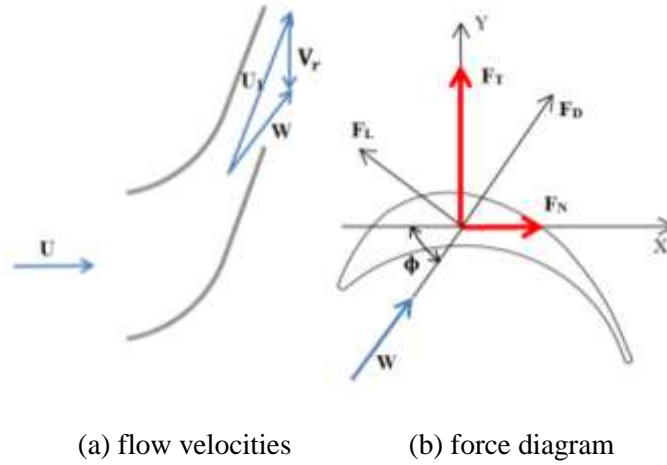(a) flow velocities   (b) force diagram
Fig. 3. Velocities and forces on a blade element.

Figure 3: Velocities and forces on a blade element: (a) flow velocities; (b) force diagram

4. Four Typical Turbulence Models
The present computational study was conducted using Finite Volume Method (FVM). Due to computational resources, four two-equation turbulence models based on the Reynolds-averaged Navier-Stokes equations were considered to choose.

4.1 Standard k- turbulence model
Launder and Spalding [15] developed the standard k-ε turbulence model based on two transport equations for turbulent kinetic energy k and its dissipation rate, ε. The eddy viscosity, μ_t, can be specified as

$$\mu_t = \rho C_\mu \frac{k^2}{\varepsilon} \tag{6}$$

$$\frac{\partial(\rho k)}{\partial t} + \text{div}(\rho k \vec{U}) = div\left(\frac{\mu}{\sigma_k} \text{ grad } k\right) + G_k - \rho\varepsilon \tag{7}$$

$$\frac{\partial(\rho k)}{\partial t} + \text{div}(\rho\varepsilon\vec{U}) = div\left(\frac{\mu}{\sigma_\varepsilon} \text{ grad } \varepsilon\right) + C_{1\varepsilon}\frac{\varepsilon}{k}G_k - C_{2\varepsilon}\rho\frac{\varepsilon^2}{k} \tag{8}$$

where σ_k and σ_ε are Prandtl numbers for the diffusivities of k and ε to the eddy viscosity, respectively, $C_{1\varepsilon}$ and $C_{2\varepsilon}$ are constants for the correct proportionality and G_k represents the generation of turbulence kinetic energy due to the mean velocity gradients. Values of constants in the standard k-ε model are suggested for turbulent flow as follows:

$$C_\mu = 0.09 \quad \sigma_k = 1 \quad \sigma_\varepsilon = 1.3 \quad C_{1\varepsilon} = 1.44 \quad C_{2\varepsilon} = 1.92$$

The standard k-ε turbulence model is the most widely used two-equation turbulence model due to its reasonable accuracy for a variety of applications. However, this turbulence model has a poor performance in some important cases such as rotating flows [17].

4.2 Realizable k- model

The realizable k-ε model is one of the most successful recent developments in all k-ε model versions [17-18]. This model contains a new transport equation for the turbulent dissipation rate and a new eddy viscosity formulation based on the realizability constraints for the turbulent viscosity. Therefore the realizable k-ε model is possible to produce better performance for flows involving separation, rotation and recirculation. The transport equations for k and ε are expressed as [21]

$$\frac{\partial(\rho k)}{\partial t} + \text{div}(\rho k \vec{U}) = div\left(\frac{\mu}{\sigma_k} \text{ grad } k\right) + G_k - \rho\varepsilon \tag{9}$$

$$\frac{\partial(\rho k)}{\partial t} + \text{div}(\rho\varepsilon\vec{U}) = div\left(\frac{\mu}{\sigma_\varepsilon} \text{ grad } \varepsilon\right) + \rho C_{1\varepsilon}E\varepsilon - \rho C_{2\varepsilon}\frac{\varepsilon^2}{k+\sqrt{v\varepsilon}} \tag{10}$$

where

$C_{1\varepsilon} = max\ [0.43, \frac{d}{d+5}]$, $d = E\frac{k}{\varepsilon}$, $E = \sqrt{2E_{ij}E_{ij}}$ and E is the modulus of the mean strain rate tensor. The constants in the realisable k- ε model are

$$\sigma_k = 1 \quad \sigma_\varepsilon = 1.2 \quad C_{2\varepsilon} = 1.9$$

4.3 Standard k-ω model

The k-ω model is the most prominent two-equation turbulence model. Wilcox [22] proposed the k-ω model which does not require wall-damping functions in low Reynolds number applications. This model is characterized by the turbulent kinetic energy k and the frequency, $\omega = \frac{k}{\varepsilon}$. The eddy viscosity is expressed by

$$\mu_t = \rho\frac{k}{\omega} \tag{11}$$

The transport equations for k and ω at high Reynolds are as follows

$$\frac{\partial(\rho k)}{\partial t} + \text{div}(\rho k \vec{U}) = \text{div}\left[\left(\mu + \frac{\mu_t}{\sigma_k}\right)\text{grad } k\right] + P_k - \beta^*\rho k\omega \tag{12}$$

$$\frac{\partial(\rho\omega)}{\partial t} + \text{div}(\rho\omega\vec{U}) = \text{div}\left[\left(\mu + \frac{\mu_t}{\sigma_\omega}\right)\text{grad }\omega\right] + \gamma_1 P_\omega - \beta_1\rho\omega^2 \tag{13}$$

where P_k and P_ω are the rate of production of k and ω, σ_k, σ_ω, β^*, β_1 and γ_1 are constants. Values for these constants are as follows:

$$\sigma_k = 2 \quad \sigma_\omega = 2 \quad \beta^* = 0.09 \quad \beta_1 = 0.075 \quad \gamma_1 = 0.553$$

4.4 SST (shear stress transport) *k-ω* model

The standard *k-ω* model does not require wall-damping functions in low Reynolds number applications [15, 20]. The near-wall performance of the standard *k-ω* model is unsatisfactory for boundary layers with adverse pressure gradients, hence Menter [21] proposed a SST (shear stress transport) *k-ω* model which uses a transformation of the *k-ε* model into the *k-ω* model in the near-wall region and keeps the standard *k-ε* model in the fully turbulent region far from the wall. The *k* equation is the same as in the standard *k-ω* model, but the *ε* equation is transformed into a ω equation by substituting ε=kω. Therefore, the SST *k-ω* model can be used without any extra damping functions in the flow region with low Reynolds number. The transport equations for *k* and *ω* are given as [16]

$$\frac{\partial(\rho k)}{\partial t} + \text{div}(\rho k\vec{U}) = \text{div}\left[\left(\mu + \frac{\mu_t}{\sigma_k}\right)\text{grad }k\right] + P_k - \beta^*\rho k\omega \tag{14}$$

$$\frac{\partial(\rho\omega)}{\partial t} + \text{div}(\rho\omega\vec{U}) = \text{div}\left[\left(\mu + \frac{\mu_t}{\sigma_{\omega,1}}\right)\text{grad }\omega\right] + \gamma_2 P_\omega - \beta_2\rho\omega^2 + 2\frac{\rho}{\sigma_{\omega,2}\omega}\frac{\partial k}{\partial x_k}\frac{\partial\omega}{\partial x_k} \tag{15}$$

where $\sigma_{\omega,1}$, $\sigma_{\omega,2}$, γ_2, β_2 are constants. Recommended values for constants in the SST *k-ω* model are as follows:

$$\sigma_k = 1; \sigma_{\omega,1} = 2; \sigma_{\omega,2} = 1.17; \gamma_2 = 0.44; \beta^* = 0.09; \beta_2 = 0.083$$

All four turbulence models, standard *k-ε*, realizable *k-ε*, standard *k-ω* and SST *k-ω* models, have been employed for wind turbines and impulse turbines [5, 22]. In order to assess the best numerical configuration, the performance of four turbulence models would be validated with the results from wind tunnel tests.

5. Computational Domain and Boundary Conditions

To investigate performances of the omni-flow wind turbine, a three-dimensional analysis was carried out with the software package: Star-CCM+. The computational domain with the wind turbine model is shown in Fig.4. The domain was 16 times the length (L) of the chamber in the axial direction, and both the domain width and height were 20 times the rotor diameter (D) of the wind turbine. Such a large domain will ensure that a blockage effect of walls does not influence the flow around the wind turbine [23]. The upstream boundary condition was set as the velocity inlet and downstream boundary condition was set as the pressure outlet, as shown in Fig. 4. Surrounding walls of the domain were specified as slip and surfaces of the wind turbine were no-slip.
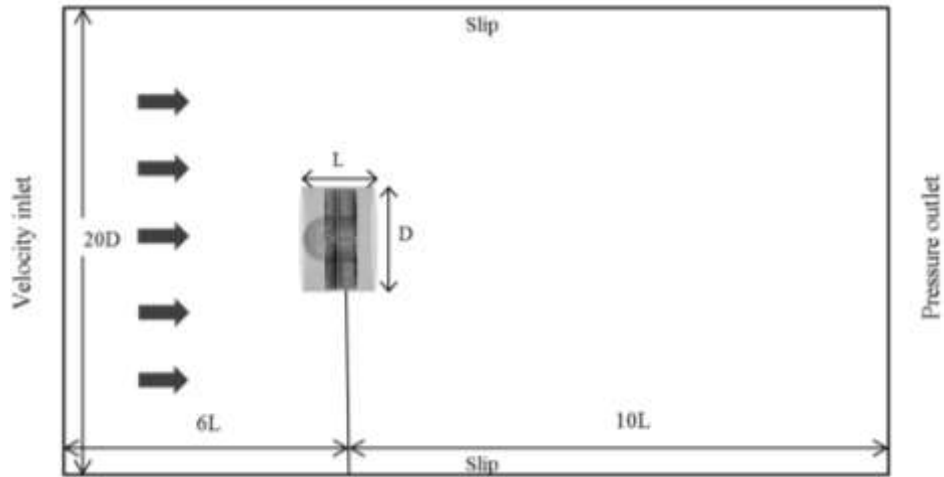
Figure 4: Schematic view of the computational domain setup in simulations [4]

Moving Reference Frame (MRF) was chosen for modelling rotational effects in this work. MRF used in investigations of wind turbines and impulse turbines has showed accurate results validated by experiments [24-25]. Sliding mesh technology has not been employed in this study because it needs more computing power for such complex 3-D geometry. Steady state was combined with the MRF in simulations. Rotational speeds were simulated from 0 rpm to 600 rpm for a free entrance stream velocity of 8.2 m/s. The value of tip speed ratio (λ) was varied by assigning different values of angular velocity as below:

$$\lambda = \omega R / U$$

The convergence to the final steady-state was assessed with a maximum amount of 2000 iterations, which was always sufficient to reach the final computed residual of 10^{-4}.

Due to the complex geometry, unstructured polyhedral cells were suitable and employed in meshing [21]. In order to obtain the dimensionless wall distance y+ < 5, the distance of the first grid layer from the blade was 0.15 mm and total 8 layers were generated with a growth rate of 1.5 [16, 24]. Fig. 5 shows the section view of the meshed model. A mesh independency test was conducted with a cell number ranging from 3,300,000 to more than 7,000,000. As shown in Fig. 6, when the cell number exceeded 6,000,000, the resulting difference between fine cells and coarse cells was less than 0.1%. Therefore, all cases in this study had around 6,000,000 polyhedral cells.
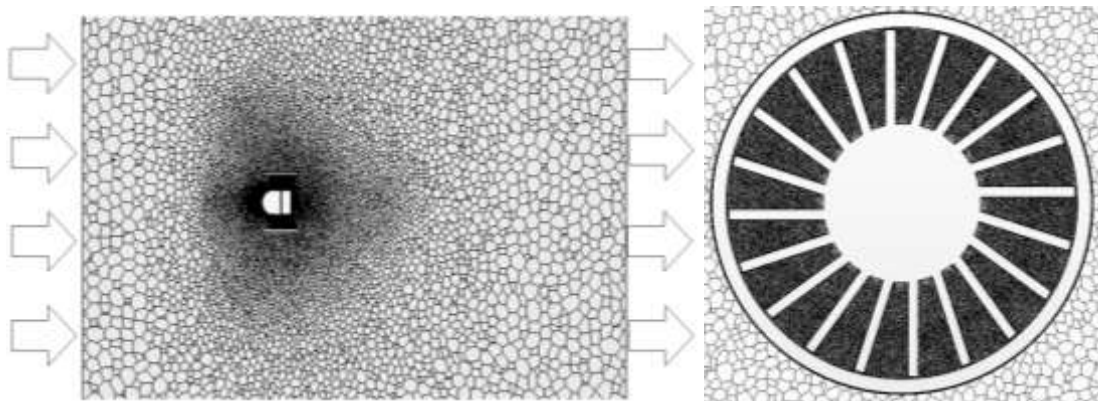

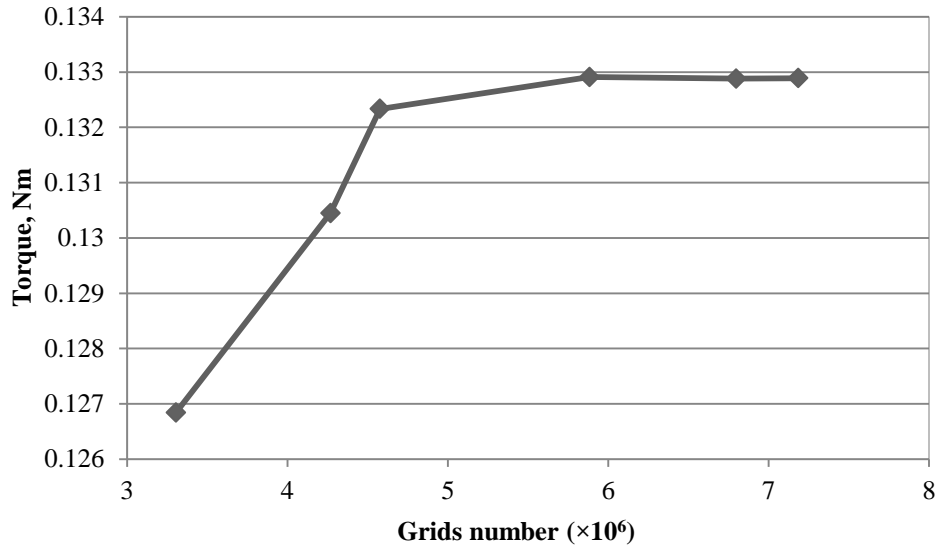**Figure 5:** Two section views of the meshed model [4].

Figure 6: Torque values under different grid numbers [4]

6. Results and Discussion

The numerical simulations were conducted with several turbulence models and the simulation results were compared with the experimental data [4] to validate the numerical approach. Four turbulence models, standard k-ε, realizable k-ε, standard k-ω and SST k-ω turbulence models, were employed to simulate the wind turbine model with 20 blades and under the condition of uniform flow. Fig. 7 shows pressure distributions surrounded a blade aerofoil under four turbulence models at a tip speed ratio of 0.76. It can be seen that all four turbulence models predicated that maximum pressures occurred on the upper blade surface near the leading edge and minimum pressures took place on the upper blade surface near the trailing edge. The maximum pressure was caused by the flow stagnation on the leading edge, where the pressure difference can result in an aerodynamics force to hinder the blade rotating. The minimum pressure was yielded due to the flow separation on the upper surface near the aerofoil rear where the pressure difference generated the major force for rotating. Compared with other turbulence models, the standard k-ε model could not predicate the minimum pressure accurately near the rear part which caused that the obtained power coefficient with this turbulence model was lower than that of others. It can also be seen that the standard k-ω and SST k-ω models both calculated the maximum pressure with lower values at the leading edge compared with that of the realizable k-ω model which resulted in less hindering forces at the leading edge and larger power coefficients.
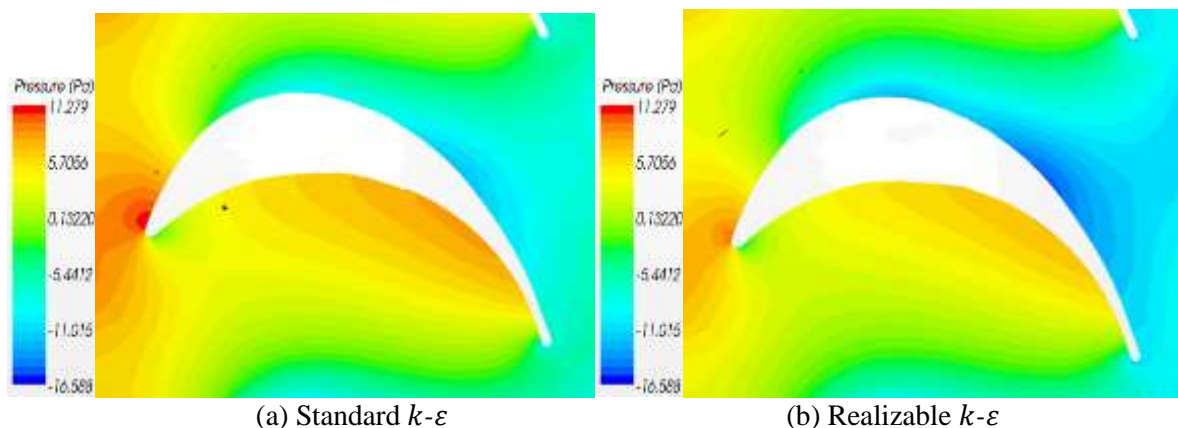
(a) Standard k-ε (b) Realizable k-ε

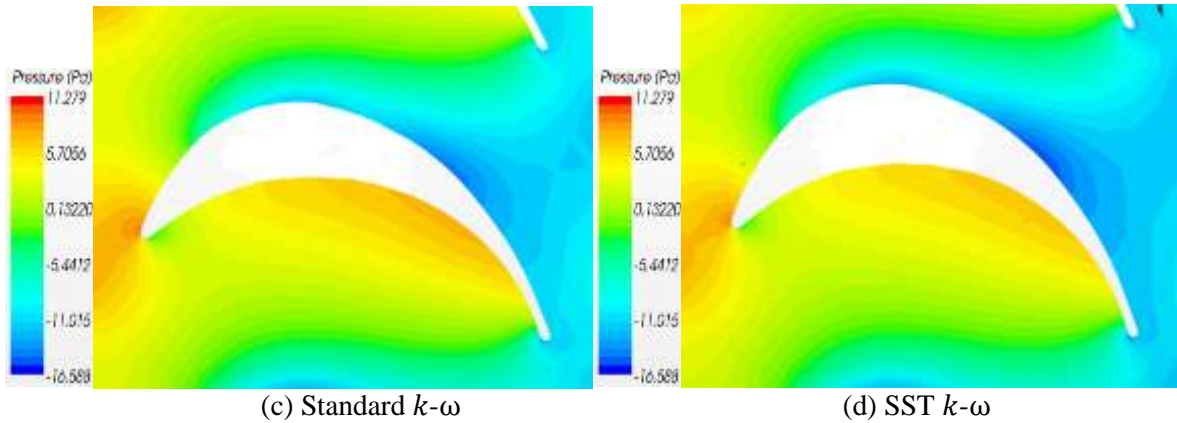(c) Standard k-ω (d) SST k-ω

Figure 7: Pressure distributions around the blade aerofoil with four turbulence models at the radius of 0.13 m
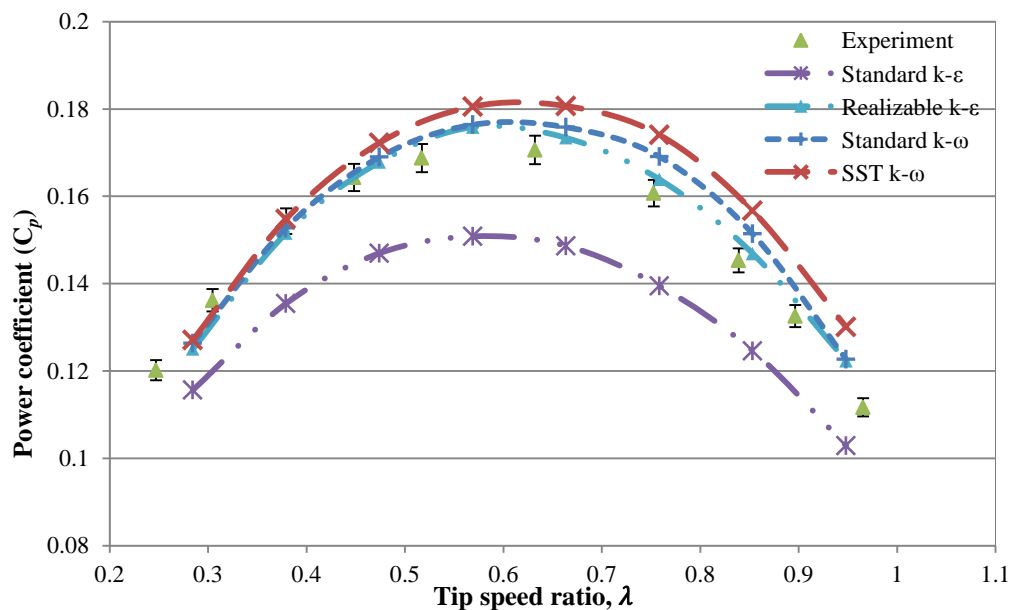

Figure 8: Power coefficient comparison with experimental data at different tip speed ratios.

Fig. 8 shows the comparison of power coefficients between the results from numerical simulation and experimental results. It can be seen that the numerical simulation results from all four turbulence models had a similar trend of power coefficient versus tip speed ratio to that from the experimental results. The error bar on experimental data represents a value of ± 1.9% of the measured value. Apart from the standard k-ε model, the numerical results from the other three models agree well with the experimental results. The standard k-ε turbulence model produced lower results compared with the experimental ones across the whole range of tip speed ratios. With the tip speed ratio exceeding 0.5, the power coefficient resulted from the SST k-ω model is about 6% higher than the experimental one. Maximum power coefficients from both the realizable k-ε model and the standard k-ω model correlated well with the maximum power coefficient from the experiment. It is suggested that the numerical approach with realizable k-ε model can provide reliable results and thus was employed for the rest of this study. The results in Fig.8 also show that the $C_p - \lambda$ curve was nearly symmetric at the tip speed ratio of 0.6 and the maximum C_p was obtained at this tip speed ratio.

7. Conclusions

An aerodynamic investigation of an omni-flow wind turbine designed for urban areas has been carried out with different numerical models. Four turbulence models in CFD simulation have been studied. Apart from Standard k-ε model, the other models have the similar trend in power coefficient against the speed tip ratio and maximum value of power coefficient occurs at the speed tip ratio of 0.6. The simulation results of this novel wind turbine from the realizable k–ε turbulence model have had a good correlation with the experimental data from wind tunnel tests. It is suggested that the realizable k-ε turbulence model is most suitable to simulate this novel wind turbine.

References

1. A. Betz. *Schraubenpropeller mit geringstem energieverlust*. Gottinger Nachr., Germany, 1919.

2. P.D. Clausen and D.H. Wood. Recent advances in small wind turbine technology. *Wind Engineering*, **24(3):** 189-201, 2000.

3. X. Zhang, *Analysis and optimisation of a novel wind turbine*. PhD thesis, University of Hertfordshire, 2013.

4. P. Ying, Y.K. Chen and Y. Xu. An aerodynamic analysis of a novel small wind turbine based on impulse turbine principles. *Renewable Energy*. **75:** 37-43, 2015.

5. L. Aresti, M. Tutar, Y. Chen and R.K. Calay. Computational study of a small scale vertical axis wind turbine (VAWT): comparative performance of various turbulence models, *Wind and Structures*. **17(6)**: 647-670, 2013.

6. E. Hau. *Wind Turbines- Fundamentals, Technologies, Applications, Economics,* 2nd edition. Berlin Hetdelberg: Springer, 2006.

7. H. Beri and Y. Yao. Effect of camber airfoil on self-starting of vertical axis wind turbine. *J. Environmental Science and Technology*, 302-312, 2011.

8. V. Sureshan. Omni-directional wind power station. Patent no. WO2008017106A1, 2008.

9. T. Setoguchi, S. Santhakumar, H. Maeda, M. Takao, K. Kaneko. A review of impulse turbines for wave energy conversion. *Renewable Energy*, **23**: 261-292, 2001.

10. V. Jayashankar, S. Anand, T. Geetha, S. Santhakumar, K.V. Jagadeesh, M. Ravindran. A twin unidirectional impulse turbine topology for OWC based wave energy plants. *Renewable Energy*, **34**: 692-698, 2009.

11. H. Maeda, M. Takao, T. Setoguchi, K. Kaneko, T.H. Kim, M. Inoue. Impulse turbine for wave power conversion with air flow rectification system. *Proceedings of the eleventh international offshore and polar engineering conference*, Stavanger, Norway, pp. 646-652, 2001.

12. T. Burton, D. Sharpe, N. Jenkins, E. Bossanyi. *Wind energy handbook*. Chichester: John Wiley & Sons, Ltd, 2001.

13. M.M. Aslam Bhutta, N. Hayat, A.U. Farooq, Z. Ali, S.R. Jamil, Z. Hussain. Vertical axis wind turbine – a review of various configurations and design techniques. *Renewable Sustainable Energy Rev*, **16**: 1926-1939, 2012.

14. J.F. Manwell, J.G. McGowan, A.L. Rogers. *Wind energy explained - theory, design and application*. Chichester, UK: John Wiley & Sons Ltd., 2002.

15. B.E. Launder and D.B. Spalding. The numerical compution of turbulent flows, *Computer Methods in Applied Mechanics and Engineering*, **3(2):** 269-289, 1974.

16. H.K. Versteeg and W. Malalasekera, *An introduction to computational fluid dynamics - the finite volume method*. Second ed., Harlow, UK: Pearson Education Ltd, 2007.

17. T. Shih, W.W. Liou, A. Shabbir, Z. Yang, and J. Zhu, A new k- eddy viscosity model for high reynolds number turbulent flows. *Computers & Fluids,* **24(3):** 227-238, 1995.

18. *Star-ccm+ user guide 6.04* 2011, New York, US: CD-adapco.

19. ANSYS, *Ansys Fluent theory guide* 2011.

20. D.C. Wilcox. Reassessment of the scale-determining equation for advanmced turbulence models. *AIAA J*, **26(11):** 1299-1310, 1988.

21. F. Menter. Two-equation eddy-viscosity turbulence model for engineering applications. *AIAA J*, **32(8):** 1598-1605, 1994.

22. A. Thakker and T.S. Dhanasekaran. Experimental and computational analysis on guide vane losses of impulse turbine for wave energy conversion. *Renewable Energy*, **30**: 1359-1372, 2005.

23. K. Abe, M. Nishida, A. Sakurai, Y. Ohya, H. Kihara, E. Wada E. Experimental and numerical investigations of flow fields behind a small wind turbine with a flanged diffuser. *J Wind Eng Ind Aerodynam*, **93**: 951-970, 2005.

24. R. Lanzafame, S. Mauro, M. Messina. Wind turbine CFD modeling using a correlation-based transitional model. *Renewable Energy*, **52**: 31-39, 2013.

25. A. Thakker and F. Hourigan. Computational fluid dynamics analysis of a 0.6m, 0.6 hub-to-tip ratio impulse turbine with fixed guide vanes. *Renewable Energy*, **30**: 1387-1399, (2005).